

RESEARCH ARTICLE | MAY 29 2012

## Magnetothermal instability in laser plasmas including hydrodynamic effects

J. J. Bissell; R. J. Kingham; C. P. Ridgers



*Phys. Plasmas* 19, 052107 (2012)

<https://doi.org/10.1063/1.4718639>



View  
Online



Export  
Citation

### Articles You May Be Interested In

Theory of the magnetothermal instability in coronal plasma flows

*Phys. Plasmas* (September 2022)

Magnetothermal instability in weakly magnetized plasmas with anisotropic resistivity and viscosity

*Phys. Plasmas* (April 2010)

Magnetothermal instability of plasmas in a horizontal magnetic field

*Phys. Plasmas* (October 2009)



**AIP Advances**

Why Publish With Us?

21 DAYS average time to 1st decision

OVER 4 MILLION views in the last year

INCLUSIVE scope

Learn More

AIP Publishing

# Magnetothermal instability in laser plasmas including hydrodynamic effects

J. J. Bissell,<sup>1,2</sup> R. J. Kingham,<sup>2</sup> and C. P. Ridgers<sup>2,3</sup>

<sup>1</sup>Department of Mathematical Sciences, University of Durham, Durham DH1 3LE, United Kingdom

<sup>2</sup>Blackett Laboratory, Imperial College London, London SW7 2BZ, United Kingdom

<sup>3</sup>Clarendon Laboratory, University of Oxford, Oxford OX1 3PU, United Kingdom

(Received 16 February 2012; accepted 24 April 2012; published online 29 May 2012)

The impact of both density gradients and hydrodynamics on the evolution of the field compressing magnetothermal instability is considered [J. J. Bissell *et al.*, Phys. Rev. Lett. **105**, 175001 (2010)]. Hydrodynamic motion is found to have a limited effect on overall growth-rates; however, density gradients are shown to introduce an additional source term corresponding to a generalised description of the field generating thermal instability [D. Tidman and R. Shanny, Phys. Fluids **17**, 1207 (1974)]. The field compressing and field generating source terms are contrasted, and the former is found to represent either the primary or sole instability mechanism for a range of conditions, especially those with Hall parameter  $\chi > 10^{-1}$ . The generalised theory is compared to numerical simulation in the context of a recent nano-second gas-jet experiment [D. H. Froula *et al.*, Phys. Rev. Lett. **98**, 135001 (2007)] and shown to be in good agreement: exhibiting peak growth-rates and wavelengths of order  $10\text{ ns}^1$  and  $50\text{ }\mu\text{m}$ , respectively. The instability's relevance to other experimental conditions, including those in inertial confinement fusion (I.C.F.) hohlraums, is also discussed. © 2012 American Institute of Physics. [<http://dx.doi.org/10.1063/1.4718639>]

## I. INTRODUCTION

The connexion between magnetic field dynamics and electron transport in laser-plasmas is both reciprocal and profound. Such interdependence has long been accounted for in classical transport theory, where, for instance, magnetic field can both suppress heat-flow and be carried with it.<sup>1,2</sup> Growing interest in the role of magnetic fields in laser-plasmas has emphasised the importance of characterising such interplay, particularly in the contexts of inertial confinement fusion (I.C.F.)<sup>3–5</sup> and magneto-inertial fusion (M.I.F.)<sup>6–8</sup> schemes but also for more general experimental topics, such as the suppression of heat transport,<sup>9</sup> the control of density channels,<sup>10</sup> and the evolution of plasma bubbles.<sup>11–13</sup>

Recently, we demonstrated that classical (Braginskii)<sup>1</sup> transport processes can lead to a new kind of instability in laser-plasmas—the field compressing *magnetothermal instability*—when heat flows perpendicular to a magnetic field  $\mathbf{B}$ .<sup>14</sup> Titled in accordance with its principal features, the magnetothermal instability compresses magnetic field, concentrates the flow of heat, and enhances thermal energy spreading (see Figure 1) and may be important when symmetry of thermal transport is a key concern, such as those contexts referred to above.<sup>3–13</sup>

The magnetothermal instability is driven by collisional transport phenomena alone and therefore of particular interest because it acts to destabilise plasmas in the absence of more usual mechanisms. In particular, unstable growth results from coupling between (i) the Nernst effect, that is, advection of  $\mathbf{B}$  with the diffusive heat-flow  $\mathbf{q}_\perp$  at velocity  $\mathbf{v}_N \approx 2\mathbf{q}_\perp/3P_e$  (where  $P_e$  is the electron pressure)<sup>2</sup> and (ii) the Righi-Leduc heat-flow, the thermal flux deflected by fields acting on negatively charged, heat-carrying electrons.<sup>1</sup> Neither density gradients (which give rise to the field generating thermal instability),<sup>15–20</sup> large anisotropies (responsible for other

heat-flux and Weibel-like instabilities),<sup>21–24</sup> nor hydrodynamic flow (necessary for interchange instabilities, such as the Rayleigh-Taylor instability and its analogues)<sup>25–27</sup> are required.

In this paper, we generalise the original theory of the magnetothermal instability<sup>14</sup> to include effects arising from both density gradients and hydrodynamics (Secs. II and III), a natural prerequisite to understanding how the instability operates under conditions for which hydrodynamic rates exceed those associated with instability. Including gradients in the electron number density  $n_e$  (i.e.,  $\nabla n_e \neq \mathbf{0}$ ) alongside those in the electron temperature  $T_e$  means that the generalised model can account for effects arising from  $\nabla T_e \times \nabla n_e$  magnetic field generation.<sup>28</sup> This is significant because coupling between the  $\nabla T_e \times \nabla n_e$  effect and the Righi-Leduc heat-flow has long been known to drive a field generating thermal instability.<sup>15–19</sup> Nearly, all existing studies of the latter assume an unmagnetised plasma, meaning that our discussion also represents a generalised description of how the field generating instability functions in the presence of existing fields: indeed, only Fruchtman and Strauss<sup>20</sup> seem to have considered magnetised conditions; nevertheless, the absence of field gradients, damping terms (such as thermal diffusion), and important advective effects from their model render its verisimilitude somewhat questionable. The theory presented here is thus essential for understanding how the mechanisms behind the magnetothermal instability and the field generating thermal instability interact (Sec. V).

We compare the generalised theory of the magnetothermal instability to numerical simulation in Sec. IV using parameters similar to those of a recent nano-second gas-jet experiment,<sup>9</sup> a context in which we find characteristic growth-rates and wavelengths of order  $10\text{ ns}^1$  and  $50\text{ }\mu\text{m}$ , respectively. Finally, in Sec. VI, we describe an approximate method for calculating peak growth-rates and wave-numbers,

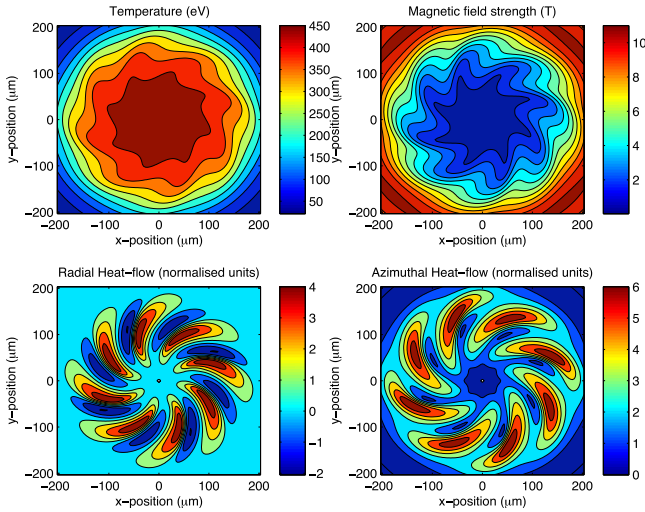


FIG. 1. Magnetothermal instability active in CTC+ simulation of the experiment by Froula *et al.*<sup>9</sup> (see Sec. IV). Here an homogeneous plasma magnetised by an 8 T field is heated for 300 ps; a 1% perturbation is then added to the field such that  $\mathbf{B} \rightarrow \mathbf{B} + \delta\mathbf{B} \sin(8\theta)$ , where  $\tan \theta = (y/x)$ , and the plasma heated for a further 160 ps, that is, 460 ps total.

which we use to assess the relevance of the instability to various experimental conditions (Sec. VII).

## II. BASIC EQUATIONS AND MAIN ASSUMPTIONS

We account for hydrodynamics using a single fluid model, neglecting electron inertia in the momentum equation and ion pressure  $P_i$  compared to electron pressure  $P_e = n_e T_e$  (with  $T_e$  in energy units). In our geometry, gradients and fluxes are taken to be perpendicular to the magnetic field  $\mathbf{B}$ , so that for scalar quantities  $f$  and vector quantities  $\mathbf{A}$  we have  $\mathbf{B} \cdot \nabla f = \mathbf{B} \cdot \mathbf{A} = 0$ . This means that magnetic tension does not contribute to magnetohydrodynamic forces, i.e.,  $(\mathbf{B} \cdot \nabla) \mathbf{B} = 0$ . The principal governing equations, the continuity equation (1), momentum equation (2), Faraday's Law (3), and the thermal energy continuity equation (4) may thus be written

$$\frac{\partial n_e}{\partial t} + \nabla \cdot (n_e \mathbf{C}) = 0, \quad (1)$$

$$\rho_i \left[ \frac{\partial \mathbf{C}}{\partial t} + (\mathbf{C} \cdot \nabla) \mathbf{C} \right] = -\nabla \left( \frac{B^2}{2\mu_0} + P_e \right), \quad (2)$$

$$\frac{\partial \mathbf{B}}{\partial t} = -\nabla \times \mathbf{E}, \text{ and} \quad (3)$$

$$\frac{3}{2} n_e \left[ \frac{\partial T_e}{\partial t} + \mathbf{C} \cdot \nabla T_e \right] + n_e T_e \nabla \cdot \mathbf{C} + \nabla \cdot \mathbf{q} - \mathbf{E}' \cdot \mathbf{j} = \dot{U}, \quad (4)$$

where  $\mathbf{E}' = \mathbf{E} + \mathbf{C} \times \mathbf{B}$  is defined by the electric field  $\mathbf{E}$  and bulk flow velocity  $\mathbf{C}$ , while  $\mathbf{q}$  is the total heat-flow,  $\rho_i = n_i m_i$  is the ion mass density (with mass  $m_i$  and number density  $n_i$ ), and  $\dot{U}$  is the rate of change of energy due to external heating. Ampère's Law is used to express the current as

$\mathbf{j} = \nabla \times \mathbf{B} / \mu_0$ . The electric field and heat-flow are calculated using Braginskii's generalised Ohm's Law and heat-flow equation, respectively,<sup>1,29–31</sup>

$$en_e \mathbf{E}' = -\nabla P_e + \mathbf{j} \times \mathbf{B} + \frac{m_e}{ec_B \tau_T} \underline{\alpha}^c \cdot \mathbf{j} - n_e \underline{\beta}^c \cdot \nabla T_e \quad (5)$$

$$\text{and } \mathbf{q} = -\frac{n_e c_B \tau_T T_e}{m_e} \underline{\kappa}^c \cdot \nabla T_e - \underline{\psi}' \cdot \mathbf{j} \frac{T_e}{e}. \quad (6)$$

Here  $c_B = 3\sqrt{\pi}/4$  is a dimensionless constant and  $e$  is the electronic charge; while the thermal collision time  $\tau_T = 4\pi v_T^3 / n_i [Ze^2 / \epsilon_0 m_e]^2 \log \Lambda_{ei}$  is defined by the thermal velocity  $v_T = (2T_e/m_e)^{1/2}$ , with  $m_e$  as the electron mass, and the Coulomb logarithm  $\log \Lambda_{ei} \approx 8$ . This allows us to further define an electron thermal mean-free-path  $\lambda_T = v_T \tau_T$ . The transport coefficients—the resistivity  $\underline{\alpha}^c$ , the thermal conductivity  $\underline{\kappa}^c$ , and the thermo-electric tensors  $\underline{\beta}^c$  and  $\underline{\psi}'$ —are dimensionless functions of the atomic number  $Z$  and Hall parameter  $\chi = c_B \omega_L \tau_T$ , where  $\omega_L = e|\mathbf{B}|/m_e$  is the electron Larmor frequency.

A unit vector in the direction of the magnetic field  $\mathbf{b} = \mathbf{B}/|\mathbf{B}|$  provides a unique reference in magnetised plasmas and transport may be split into components parallel and perpendicular to field lines. Indeed, for a general transport coefficient  $\underline{\eta}$  and driving force  $\mathbf{s}$ , in our geometry ( $\mathbf{B} \cdot \nabla f = \mathbf{B} \cdot \mathbf{A} = 0$ ) we have  $\underline{\eta} \cdot \mathbf{s} = \eta_\perp \mathbf{s} \pm \eta_\parallel \mathbf{b} \times \mathbf{s}$ , where the components  $\eta_\perp$  and  $\eta_\parallel$  may be expressed as rational polynomial fits with  $\chi$  for different values of  $Z$ ,<sup>30,31</sup> and the sign of the last term is only negative for the conductivity  $\underline{\alpha}^c$ . When data are presented here, we assume the Lorentz approximation, i.e., polynomial fits with  $Z \rightarrow \infty$ . Note that  $\underline{\psi}'$  accounts for the relationship  $\mathbf{q} \approx \mathbf{q}_e - (5T_e)/(2e)\mathbf{j}$  between the total heat-flow  $\mathbf{q}$  and the intrinsic heat-flow  $\mathbf{q}_e$ ,<sup>32</sup> so that  $\underline{\psi}' = \underline{\psi}^c + (5/2)\underline{\mathbb{I}}$ , where  $\underline{\psi}^c = \underline{\beta}^c$  and  $\underline{\mathbb{I}}$  is the identity tensor. Combining Eqs. (3) and (5), to form the induction equation, and substituting for  $\mathbf{q}$  and  $\mathbf{E}$  in the energy continuity equation (4) thus provides a complete description of the principal quantities  $T_e$ ,  $\mathbf{B}$ ,  $n_e$ , and  $C$ .

The handling of terms relating to collisional transport is made more amenable by associating diffusive and advective effects with dimensionless coefficients symbolised by the letters  $D$  and  $A$ , respectively. More specifically, we employ the following coefficients defined in Table I and motivated by Bissell:<sup>33</sup>  $D_T$ , the thermal diffusion coefficient;  $D_R$ , the resistive diffusion coefficient;  $A_N$ , the “Nernst advection coefficient;” and  $A_E$ , the “Ettingshausen advection coefficient.” Two further dimensionless coefficients defined in Table I are also used:  $C_\kappa$ , the Righi-Leduc heat-flow coefficient; and  $C_G$ , a coefficient associated with  $\nabla T_e \times \nabla n_e$  field generation. This notation permits the “tracking” of key transport phenomena and aids economy of expression in the analysis.<sup>33</sup>

Before proceeding with the linear perturbation theory, note that in what follows we assume the square of the sound speed  $v_s$  to greatly exceed that of the Alfvén speed  $v_A$ , i.e.,  $v_s^2/v_A^2 \gg 1$ , where  $v_A^2 = (B^2/\rho_i \mu_0)$  and  $v_s^2 = (\gamma_c P_e/\rho_i)$ , with

TABLE I. Dimensionless notation for effects arising from both collisional transport and the  $\nabla T_e \times \nabla n_e$  mechanism.<sup>33</sup> Note that  $\Lambda = \lambda_T/\delta$  is the ratio of the mean-free-path  $\lambda_T$  to the collisionless-skin-depth  $\delta = c/\omega_{pe}$ , where  $c$  is the speed of light *in vacuo* and  $\omega_{pe} = (n_e e^2 / \epsilon_0 m_e)^{1/2}$  is the plasma frequency.

Dimensionless coefficient	Definition
Thermal diffusion	$D_T = \frac{c_B}{3} \kappa_\perp$
Resistive diffusion	$D_R = \frac{\alpha_\perp}{c_B \Lambda^2}$
Nernst advection	$A_N = \frac{c_B}{2\chi} \beta_\wedge$
Ettingshausen advection	$A_E = \frac{2\chi\psi_\wedge}{3c_B \Lambda^2}$
Righi-Leduc heat-flow	$C_\kappa = \frac{c_B}{3} \chi \frac{\partial \kappa_\wedge}{\partial \chi}$
B-field generation by $\nabla T_e \times \nabla n_e$	$C_G = \frac{c_B}{2\chi}$

$\gamma_c = 5/3$  as the ratio of specific heats. In essence, such an assumption is equivalent to demanding that the thermal pressure  $P_e = n_e T_e$  is much greater than the magnetic pressure  $P_B = B^2/2\mu_0$ , that is,  $\beta \gg 1$  or

$$\beta = \frac{P_e}{P_B} = \frac{2}{\gamma_c} \frac{v_s^2}{v_A^2} = \frac{c_B^2 \Lambda^2}{\chi^2} \gg 1, \text{ where } \Lambda = \frac{\lambda_T}{\delta},$$

with  $\delta = \frac{c}{\omega_{pe}}$  and  $\omega_{pe} = \left( \frac{n_e e^2}{\epsilon_0 m_e} \right)^{1/2}$  (7)

as the collisionless-skin-depth and plasma frequency, respectively, and  $c$  as the speed of light *in vacuo*. In addition, we employ the inequality  $\Lambda \gg 1$ , which holds for relatively hot, low density plasmas (see Eq. (36)), combining it with condition (7) to form the stronger assumption

$$\Lambda^2 \gg \max\{1, \chi^2\}. \quad (8)$$

This inequality is key to simplifying our description and permits the neglect of a number of somewhat awkward terms in the analysis: first, non-linear terms arising from Ohmic heating; second, in combination with the local approximation (see Sec. III), terms in  $\beta_\perp$  and  $\alpha_\wedge$ ; third, contributions from the Hall field  $\mathbf{j} \times \mathbf{B}$  when compared to those due to field generation by  $\nabla T_e \times \nabla n_e$ ; fourth, heat-flow advection associated with the current (e.g., terms in  $\psi_\perp$ ); and fifth (in effect), magnetic pressure compared to thermal pressure in the momentum equation (2).

### III. LINEAR PERTURBATION THEORY

We now consider the stability of Eqs. (1)–(4) in a Cartesian  $(x, y, z)$  geometry with  $\mathbf{B} = B\hat{\mathbf{z}}$ , where  $\hat{\mathbf{z}}$  is a unit vector in the  $z$ -direction and the parameter  $\sigma_B = B/|B|$  may be used to describe whether the field is aligned parallel ( $\sigma_B = 1$ ) or antiparallel ( $\sigma_B = -1$ ) to the  $z$ -axis. In zeroth-order, we assume solutions for the principal quantities  $T_e = T_0(x, t)$ ,  $B = B_0(x, t)$ ,  $n_e = n_0(x, t)$ , and  $\mathbf{C} = C_0(x, t)\hat{\mathbf{x}}$ , where  $\hat{\mathbf{x}}$  is a unit vector in the  $x$ -direction, and define length scales  $l_f$  through the relation

$$\frac{1}{l_f} = \frac{1}{f_0} \frac{\partial f_0}{\partial x}, \text{ where } f_0 \in \{T_0, B_0, n_0, C_0\}, \quad (9)$$

a form permitting negative values. To the zeroth-order solutions we add wavelike perturbations with wavevector  $\mathbf{k}$  and frequency  $\omega$ , propagating at an angle  $\theta$  to the  $x$ -axis of the system such that  $\mathbf{k} = k \cos \theta \hat{\mathbf{x}} + k \sin \theta \hat{\mathbf{y}}$ , where  $k = |\mathbf{k}|$  and  $\hat{\mathbf{y}}$  is a unit vector in the  $y$ -direction. Hence,

$$T_e = T_0 + \delta T, \quad \delta T = \delta T' \exp[i(\mathbf{k} \cdot \mathbf{r} - \omega t)], \quad (10a)$$

$$B = B_0 + \delta B, \quad \delta B = \delta B' \exp[i(\mathbf{k} \cdot \mathbf{r} - \omega t)], \quad (10b)$$

$$n_e = n_0 + \delta n, \quad \delta n = \delta n' \exp[i(\mathbf{k} \cdot \mathbf{r} - \omega t)], \quad (10c)$$

$$\mathbf{C} = C_0 \hat{\mathbf{x}} + \delta \mathbf{C} \hat{\mathbf{k}}, \quad \delta \mathbf{C} = \delta \mathbf{C}' \exp[i(\mathbf{k} \cdot \mathbf{r} - \omega t)], \quad (10d)$$

where  $\delta T'$ ,  $\delta B'$ ,  $\delta n'$ , and  $\delta \mathbf{C}'$  are complex,  $\mathbf{r} = x \hat{\mathbf{x}} + y \hat{\mathbf{y}}$  and  $\hat{\mathbf{k}} = \mathbf{k}/k$ . We assume the local conditions  $|kl_f| \gg 1$  and  $|\nabla l_f^{-1}| \lesssim 1/l_f^2$  throughout.

For convenience, we further define a dimensionless frequency  $\Omega = \omega \tau_T$  and dimensionless wave-number  $K = k \lambda_T$ , alongside a characteristic dimensionless velocity

$$V = (\Omega/K) - C_\Theta, \text{ where } C_\Theta = (C_0/v_T) \cos \theta \quad (11)$$

is the component of the bulk flow moving parallel to the perturbation (i.e., Doppler shift) normalised to the thermal velocity  $v_T$ . Finally, we employ the dimensionless sound speed  $V_s = v_s/v_T$  and length scales  $L_f = l_f/\lambda_T$ . This additional notation is summarised in Table II.

Thus—after substituting the perturbed forms of Eq. (10a) into Eqs. (1)–(4), subtracting the zeroth-order solutions and neglecting appropriate terms—to first-order we obtain a quartic dispersion relation in  $\Omega$  and a sextic in  $K$ , that is,<sup>33</sup>

---


$$V^2 \left\{ V^2 + [(iKD_T - V_B) + iKD_R]V + \left[ (iKD_T - V_B)iKD_R + \frac{1}{4}S_G - \frac{1}{4}S_P iK + \frac{1}{4}S_E K^2 \right] \right\} - V_s^2 \left\{ V^2 + \left[ \frac{3}{5}(iKD_T - V_B) + iKD_R \right] V + \left[ \frac{3}{5}(iKD_T - V_B)iKD_R + \frac{3}{20}\Lambda_G S_G - \frac{3}{20}S_P iK + \frac{3}{20}S_E K^2 \right] \right\} = 0, \quad (12)$$

TABLE II. Dimensionless parameters used in linear theory.

Dimensionless parameter	Definition
Perturbation frequency	$\Omega = \omega\tau_T$
Perturbation wave-number	$K = k\lambda_T$
Sound speed	$V_s = v_s/v_T$
Length-scale of scalar $f_0 \in \{T_0, B_0, n_0\}$	$L_f = l_f/\lambda_T$

where the dimensionless velocity  $V_B$ , source terms  $S_G, S_P$ , and  $S_E$ , and parameters  $\Lambda_G$  and  $\Lambda_B$  are defined

$$S_G = 4 \frac{C_\kappa C_G}{L_T L_n} \sin^2 \theta, \quad S_P = 4 A_N \frac{\sigma_B}{L_T} C_\kappa \sin \theta, \quad (13)$$

$$S_E = 4 A_N A_E, \quad V_B = \frac{S_P L_T}{4 A_N L_B} \Lambda_B, \quad (14)$$

$$\Lambda_G = \left( 1 + \frac{L_n}{L_T} \right) \text{ and } \Lambda_B = \left( 1 - \frac{L_B}{L_n} \right). \quad (15)$$

The quartic nature of the dispersion relation precludes meaningful direct solution, and for this reason it is expedient to define two limiting regimes before discussing the meaning of the various terms. Indeed, writing Eq. (12) as we have done, an expression constituting two terms in curly brackets of similar magnitude, suggests two limits for which approximate solutions may be found. More specifically, by defining both a *classical transport* (CT) and an *hydrodynamical* (HD) regime (cf. Hirao and Ogasawara),<sup>19</sup> i.e.,

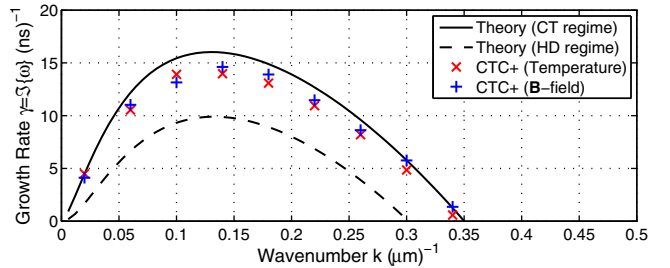


FIG. 2. Dispersion relations for unstable modes calculated from one-dimensional CTC+ simulation profiles of a 6 T magnetised plasma (see Sec. IV). The curves correspond to predictions in both the classical transport (solid curve) and the hydrodynamical (dashed curve) regimes described in Secs. III A and III B respectively. Growth-rates of the thermal and field perturbations measured from two-dimensional perturbed simulations (red and blue crosses, respectively) are also included (see Sec. IV). The data used to calculate the theoretical curves are summarised in Table III.

$$\text{Classical transport (CT) regime : } V^2 \gg V_s^2 \quad (16)$$

$$\text{and Hydrodynamical (HD) regime : } V^2 \ll V_s^2, \quad (16b)$$

the quartic dispersion relation may be approximated as a quadratic comprising either the first (CT regime) or second (HD regime) term in curly brackets and solved accordingly (see Figures 2 and 3). These regimes provide a more natural context in which to discuss the generalised theory of the magnetothermal instability and shall be considered further in the following subsections. Using the subscripts “CT” and “HD” to refer to solutions for  $\Omega$  in the classical transport and hydrodynamical limits respectively, the dispersion relations relevant to each are

$$\Omega_{\text{CT}} = \frac{1}{2} \left\{ (V_B + 2C_\Theta)K - (D_T + D_R)iK^2 \pm \sqrt{[(D_T - D_R)iK^2 - V_B K]^2 - S_G K^2 + S_P iK^3 - S_E K^4} \right\} \text{ and} \quad (17)$$

$$\Omega_{\text{HD}} = \frac{1}{2} \left\{ \left( \frac{3}{5}V_B + 2C_\Theta \right)K - \left( \frac{3}{5}D_T + D_R \right)iK^2 \pm \sqrt{\left[ \left( \frac{3}{5}D_T - D_R \right)iK^2 - \frac{3}{5}V_B K \right]^2 - \frac{3}{5}\Lambda_G S_G K^2 + \frac{3}{5}S_P iK^3 - \frac{3}{5}S_E K^4} \right\}. \quad (18)$$

## A. CT regime

The positive root of the CT dispersion relation (Eq. (17)) yields unstable solutions  $\Im\{\Omega_{\text{CT}}\} > 0$  for real wave-numbers up to a cut-off  $K_{\text{CT}}$  defined by

$$K_{\text{CT}}^2 = \left[ \frac{S_P^2}{4} \left( 1 + \frac{D_R L_T}{A_N L_B} \Lambda_B \right) \left( 1 - \frac{D_T L_T}{A_N L_B} \Lambda_B \right) \times \left( \frac{1}{D_T + D_R} \right)^2 + S_G \right] \left[ \frac{1}{4 D_T D_R - S_E} \right]. \quad (19)$$

In the absence of density gradients and hydrodynamics ( $L_n \rightarrow \infty, S_G = 0$  and  $\Lambda_B = 1$ ), the definition of the cut-off wave-number reduces to that of our previous description<sup>14</sup>

(see Eq. (30), Sec. VI), in which case the various terms in Eq. (17) may be understood as follows. At relatively low  $K$ , perturbations grow primarily as a result of feedback between the Nernst effect ( $A_N$ ) and the Righi-Leduc heat-flow ( $C_\kappa$ ) accounted for by the principal source term  $S_P \propto A_N C_\kappa$ . Since this term is proportional to  $K^3$  and occurs *within* the square-root, it yields growth that goes as  $K^{3/2}$ . The main damping terms arising from thermal ( $D_T$ ) and resistive ( $D_R$ ) diffusion, however, are proportional to  $K^2$  and only out-compete the source term at higher wave-numbers. Thus, the form of the dispersion curves in Figures 2 and 3: the growth-rate increases with  $K$  up to some maximum and then decreases to zero at a cut-off wave-number for which the source and diffusive terms are exactly matched. Notice that the angular

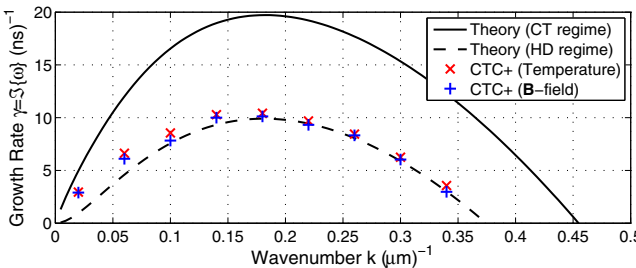


FIG. 3. Dispersion relations for unstable modes calculated from one-dimensional CTC+ simulation profiles of a 12 T magnetised plasma (see Sec. IV). As in Figure 2, the curves correspond to predictions in both the classical transport (solid curve) and the hydrodynamical (dashed curve) regimes; while growth-rates of the thermal and field perturbations measured from two-dimensional perturbed simulations (red and blue crosses, respectively) are also included (see Sec. IV). The data used to calculate the theoretical curves in this case are also summarised in Table III.

dependence of  $S_P$  means that a  $y$ -component to the perturbation is needed for instability; consequently, in the simulation results presented in Sec. IV, we take  $\theta = \pi/2$ , i.e.,  $\sin \theta = 1$ .

The velocity term  $V_B$  can enhance instability by modifying the phase between thermal and field perturbations, but is understood to be inessential because solutions with  $\Im\{\Omega_{CT}\} > 0$  exist even when  $V_B = 0$ : a feature of Eq. (17) not replicated if  $S_P = 0$ . Similarly, the source term  $S_E \propto A_N A_E$ , which describes feedback between the Nernst ( $A_N$ ) and Ettingshausen ( $A_E$ ) effects, cannot itself drive unstable waves, but provides an important contribution to instability by reducing the impact of diffusion in the denominator of final term of Eq. (19).

The net effect of density gradients in the CT regime, therefore, is to modify  $V_B$  by the factor  $\Lambda_B$  (accounting for additional divergence in the Righi-Leduc heat-flow) and to introduce a new source term  $S_G \propto C_G C_k$  describing feedback between the Righi-Leduc heat-flow ( $C_k$ ) and field generation ( $C_G$ ) from the temperature perturbation ( $\nabla \delta T \times \nabla n_0$ ).<sup>33</sup> Of these, the introduction of  $S_G$  is by far the most important since it represents the contribution to instability arising from the field generating thermal instability mechanism.<sup>15–19</sup> That  $S_G$  should be identified with the field generating source term may be justified by considering the low-field limit  $\chi \rightarrow 0$  with  $\theta = \pi/2$ ; in this case, the CT dispersion relation reduces to that of the field generating instability described by Tidman and Shanny,<sup>15</sup> and the square of the cut-off becomes

$$K_G^2 = \lim_{\chi \rightarrow 0} K_{CT}^2 = \frac{S_G}{4D_T D_R} = \frac{1}{4D_T D_R} \left( \frac{2c_B^2}{3L_T L_n} \frac{\partial \kappa_\wedge}{\partial \chi} \right). \quad (20)$$

Since we require the cut-off wave-number to be real ( $K_G^2 > 0$ ), we thereby recover the well-known result for unmagnetised conditions ( $\chi = 0$  and  $\partial \kappa_\wedge / \partial \chi > 0$ ) that the field generating source  $S_G$  can drive instability when temperature and density length-scales are parallel, i.e.,  $L_T L_n > 0$ . And in a magnetised plasma, with  $\chi \gtrsim 1$  and  $\partial \kappa_\wedge / \partial \chi < 0$ , the same term drives instability when  $L_T L_n < 0$ . [A result first noted by Fruchtman and Strauss.<sup>20</sup> Nevertheless, by neglecting diffusive and advective effects, these authors failed to specify both the forms of the cut-off wave-number  $K_{CT}$  and the role of damping

terms, and completely missed the significance of the magnetothermal source term  $S_P$ .] In general, however, the combined effect of the magnetothermal and field-generating source terms under magnetised conditions must be understood from the definition of the cut-off wave-number  $K_{CT}$  in Eq. (19): the field generating source  $S_G$  combines with the magnetothermal source  $S_P$  to enhance instability (that is, greater  $K_{CT}^2$ ) whenever  $S_G > 0$ , counteracting it otherwise ( $S_G < 0$ ).

## B. HD regime

As with the CT dispersion relation in Sec. III A, the positive root to the dispersion relation in the hydrodynamical regime (Eq. (18)) yields unstable solutions for a range of  $K$  up to a cut-off wave-number, which in this case is labelled  $K_{HD}$  and defined by

$$K_{HD}^2 = \left[ \frac{3S_P^2}{5} \left( 1 + \frac{D_R L_T}{A_N L_B} \Lambda_B \right) \left( 1 - \frac{3D_T L_T}{5A_N L_B} \Lambda_B \right) \right. \\ \left. \times \left( \frac{1}{\frac{3}{5}D_T + D_R} \right)^2 + \Lambda_G S_G \right] \left[ \frac{1}{4D_T D_R - S_E} \right]. \quad (21)$$

The similarity between the form of  $\Omega_{CT}$  and  $\Omega_{HD}$ , and the cut-offs  $K_{CT}$  and  $K_{HD}$ , indicates that instability growth-rates are comparable in both classical transport and hydrodynamical regimes: a feature evident in the dispersion curves of Figures 2 and 3. Indeed, aside from the factors of  $\frac{3}{5} = \gamma_c^{-1}$ , where  $\gamma_c$  is the ratio of specific heat capacities for an ideal gas, the only new feature of Eq. (18) compared to Eq. (17) is the introduction of a parameter  $\Lambda_G = (1 + L_n/L_T)$ . This term is a direct consequence of the introduction of density perturbations  $\delta n \neq 0$  in our hydrodynamical analysis: multiplying by  $\Lambda_G$  ensures that the field generating source term  $S_G$  accounts for generation due to both  $\nabla \delta T \times \nabla n_0$  and  $\nabla T_0 \times \nabla \delta n$  in the  $\nabla T_e \times \nabla n_e$  mechanism. [This effect was first noted by Ogasawara *et al.*<sup>18</sup> and means that the field generating thermal instability can be active in unmagnetised plasmas, for which  $\chi = 0$  and  $\partial \kappa_\wedge / \partial \chi > 0$ , when  $L_T L_n < 0$ .] However, by the form of the cut-off  $K_{HD}$  defined in Eq. (21), we find that in the HD regime the field generating source  $S_G$  will only combine with the magnetothermal source  $S_P$  to drive instability provided  $\Lambda_G S_G > 0$ . Hence, because  $\Lambda_G$  can have the opposite sign to  $S_G$ , the field generating source can have a stabilising effect on the magnetothermal instability ( $\Lambda_G S_G < 0$ ) in the HD regime regardless of whether it enhances instability in the CT limit with  $S_G > 0$ , and *vice versa*. This result is particularly important for experimental contexts in which the magnetothermal mechanism is thereby rendered the sole source of instability (see Sec. V).

## IV. COMPARISON WITH SIMULATION

Given the assumptions made in our generalised linear theory, it is instructive to compare theoretical growth-rates with those measured from simulation of the magnetothermal instability in an experimental context. To this end—as in our original paper—we consider conditions based on the investigation by Froula *et al.* into the suppression of non-local transport by magnetic fields.<sup>9</sup> However, in this paper, we compare

TABLE III. Summary of data used to generate the dispersion curves in Figures 2 and 3 for both the CT and HD regimes. Here the first column labelled “Field” refers to the initial uniform magnetic fluxdensity  $|\mathbf{B}|$  applied at time  $t = 0$ , while the  $x$ -position of the cross-section is  $x = 120 \mu\text{m}$  in each case. The data in this table are derived from snapshots taken after 500 ps of laser heating for the 6 T plasma and 700 ps for the 12 T plasma.

Field	$T_e/\text{keV}$	$n_e/10^{21}\text{cm}^{-3}$	$l_T/\mu\text{m}$	$l_B/\mu\text{m}$	$l_n/\mu\text{m}$	$\chi$	$\Lambda$
6 T	0.392	0.0149	-190	129	592	2.4	20.5
12 T	0.436	0.0142	-152	152	235	6.1	26.0

numerical results with dispersion relations from both the CT and HD regimes, Eqs. (17) and (18) respectively, and use CTC+, our transport code with coupled magnetohydrodynamic motion, as the primary numerical tool (i.e., rather than our purely transport code CTC, see Sec. VII). In Froula’s experiment, a nitrogen gas-jet ( $Z = 7$ ) of number density  $n_e = 1.5 \times 10^{19} \text{ cm}^{-3}$  and initial temperature  $T_e = 20 \text{ eV}$  was subject to long-pulse ( $> 1\text{ ns}$ ) inverse-bremsstrahlung heating by a laser of wavelength 1054nm and intensity  $6.3 \times 10^{14} \text{ Wcm}^{-2}$  focused to a  $150 \mu\text{m}$  diameter spot. Uniform magnetic fields of strengths up to 12T were imposed parallel to the heating beam, and the radial heat-flow inferred from temperature and density measurements. These parameters should be assumed in what follows; however, because our linear theory is based on a planar  $x$ - $y$  geometry, we simulate a laser heating “strip” rather than a circular spot, using a heating operator  $U_L(x)$  that is a function of  $x$ -position only (cf. Bissell *et al.*).<sup>14</sup>

The dependence of the  $D_{T,R}, V_B$ , and  $S_{G,P,E}$  coefficients on the zeroth-order principal quantities  $T_0(x,t), B_0(x,t)$ , and  $n_0(x,t)$  means that instability growth-rates vary temporally and spatially. Evaluation of the dispersion relation is thus limited to a particular cross-section through the plasma at a particular time, and hence on a unique snapshot of the bulk profile (see Table III).<sup>33</sup> Furthermore, the generalised theory of the magnetothermal instability yields two dispersion curves for any given profile—one for each of the CT or HD regimes defined in Eqs. (16)—and it should be noted that neither may necessarily correspond exactly to the actual plasma conditions. Nevertheless, the instability growth-rates  $\gamma = \Im\{\omega\}$  determined from simulation results may be used in place of the complex frequency  $\omega = \Omega/\tau_T$  to estimate how far either of these conditions hold. Indeed, for the data in Figure 2, simulation indicates a peak wave-number  $k_M$  and growth-rate  $\gamma_M(k_M)$  such that (see Table IV)

$$\gamma_M^2/v_s^2 k_M^2 = \Gamma_M^2/V_s^2 K_M^2 \approx 0.37 \lesssim 1, \quad (22)$$

TABLE IV. Comparison between the peak growth-rate  $\gamma_M = \Im\{\omega(k_M)\}$  and characteristic hydrodynamic rate  $k_M v_s$  measured from simulation in Figures 2 and 3 (where  $k_M$  is the peak wave-number and  $v_s$  is the sound speed). In both figures, computational data are taken from the cross-section  $x = 120 \mu\text{m}$  used to evaluate the dispersion relations (see Table III).

Reference	$v_s/\text{kms}^{-1}$	$k_M/\mu\text{m}^{-1}$	$\gamma_M/\text{ns}^{-1}$	$(\gamma_M/k_M v_s)^2$
Figure 2	177	$\approx 0.14$	$\approx 15$	$\approx 0.37$
Figure 3	187	$\approx 0.18$	$\approx 10$	$\approx 0.09$

where  $\Gamma_M = \gamma_M \tau_T$ , so that neither hydrodynamic nor instability rates dominate dynamics: the plasma is intermediate between the two regimes. Nevertheless, for the simulation data in Figure 3, we have (again, see Table IV)

$$\gamma_M^2/v_s^2 k_M^2 = \Gamma_M^2/V_s^2 K_M^2 \approx 0.09 \ll 1 \quad (23)$$

indicating relative dominance of hydrodynamic rates and association with the HD regime. With inequalities (22) and (23) mind, the CTC+ numerical data in Figures 2 and 3 lend compelling support to our theoretical analysis: measured rates lie broadly between the CT and HD curves in Figure 2, and are more closely aligned with the HD curve in Figure 3.

## V. PRINCIPAL INSTABILITY MECHANISM

Since the inclusion of density gradients and hydrodynamics into our generalised theory yields both field compressing (magnetothermal) and field generating source terms,  $S_P$  and  $S_G$ , respectively, it is appropriate to consider how the two mechanisms compare. Indeed, we have already seen that by increasing the magnitude of the respective cut-off wave-numbers, field generation enhances instability in the CT regime whenever  $S_G > 0$  (Sec. III A), and in the HD regime when  $\Lambda_G S_G > 0$  (Sec. III B). Consequently, and as we shall now demonstrate, comparing the magnitude of each mechanism’s contribution to the cut-offs  $K_{\text{CT}}$  and  $K_{\text{HD}}$  provides a natural means of assessing their relative dominance.

Before proceeding, note that  $A_N \approx D_T$ , so from our assumption  $\Lambda^2 \gg \max\{1, \chi^2\}$ , we have (see Figure 4)

$$A_N \approx D_T \gg D_R. \quad (24)$$

If we assume  $|L_B| \gtrsim |L_T|$ , this inequality means that we can define characteristic wave-numbers  $K_{\text{PCT}}$  and  $K_{\text{PHD}}$  describing the approximate contributions to the cut-off wave-numbers from the magnetothermal mechanism ( $S_P$ ) in the CT and HD regimes, respectively,

$$K_{\text{PCT}}^2 = \frac{C_\kappa^2 \sin^2 \theta}{L_T^2} \left( 1 - \frac{L_T}{L_B} \Lambda_B \right) \left( \frac{4}{4D_T D_R - S_E} \right),$$

$$K_{\text{PHD}}^2 = \frac{5C_\kappa^2 \sin^2 \theta}{3L_T^2} \left( 1 - \frac{3L_T}{5L_B} \Lambda_B \right) \left( \frac{4}{4D_T D_R - S_E} \right). \quad (25)$$

Indeed, by these definitions, the total cut-off wave-numbers of Eqs. (19) and (21) may be approximated

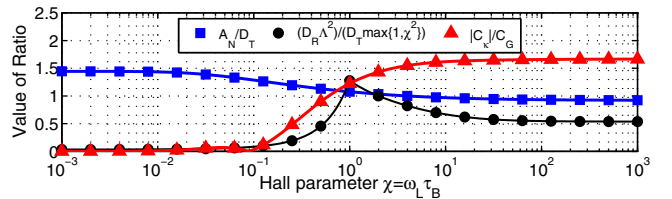


FIG. 4. The ratios  $A_N/D_T$ ,  $(D_R \Lambda^2)/(D_T \max\{1, \chi^2\})$  and  $|C_k|/C_G$  plotted for a range of Hall parameters. From these curves, inequality (24) may be understood as follows. First, since  $A_N/D_T \approx 1$  (blue curve, square markers), we have  $A_N \approx D_T$ . Second, because  $(D_R \Lambda^2)/(D_T \max\{1, \chi^2\}) \lesssim 1$  (black curve, circular markers), our initial assumption  $\Lambda^2 \gg \max\{1, \chi^2\}$  implies  $D_R/D_T \lesssim \max\{1, \chi^2\}/\Lambda^2 \ll 1$ , that is,  $D_T \gg D_R$ .

$$K_{CT}^2 \approx K_{PCT}^2 + K_G'^2 \text{ and } K_{HD}^2 \approx K_{PHD}^2 + \Lambda_G K_G'^2, \quad (26)$$

where  $K_G'$  is the contribution from the field generating source term, i.e.,

$$K_G'^2 = \frac{C_\kappa C_G \sin^2 \theta}{L_T L_n} \left( \frac{4}{4D_T D_R - S_E} \right), \quad (27)$$

and as such tends to  $K_G$  in the low  $\chi$  limit (see Eq. (20)). Broadly speaking, this means that the magnetothermal mechanism dominates over the field generating mechanism in the classical transport regime when

$$\frac{|K_{PCT}^2|}{|K_G'^2|} = \left| \frac{C_\kappa}{C_G} \left( \frac{L_n}{L_T} - \frac{L_n}{L_B} + 1 \right) \right| > 1 \quad (28)$$

and in the hydrodynamical regime if

$$\frac{|K_{PHD}^2|}{|\Lambda_G K_G'^2|} = \left| \frac{C_\kappa}{C_G} \left( \frac{5L_n}{3L_T} - \frac{L_n}{L_B} + 1 \right) \left( \frac{L_T}{L_T + L_n} \right) \right| > 1, \quad (29)$$

where the ratio  $|C_\kappa/C_G|$  is plotted in Figure 4. Evaluating these ratios using the scale-lengths and Hall parameters given in Table III, we find  $|K_{PCT}^2/K_G'^2| \approx 8.5$  and  $|K_{PHD}^2/\Lambda_G K_G'^2| \approx 5.2$  for the dispersion curves in Figure 2, while  $|K_{PCT}^2/K_G'^2| \approx 3.1$  and  $|K_{PHD}^2/\Lambda_G K_G'^2| \approx 8.5$  for the curves in Figure 3, that is, the magnetothermal mechanism takes a share of the overall cut-off by between  $\sim 75\%$  and  $\sim 90\%$ . Under the conditions of Froula *et al.* considered here,<sup>9</sup> such dominance by the magnetothermal source in the hydrodynamical regimes is in fact necessary for instability, since in these cases the field generating mechanism acts to suppress the growth of unstable modes, i.e.,  $\Lambda_G S_G < 0$ . However, the ratio  $|C_\kappa/C_G|$  is small at low values of the Hall parameter  $\chi$  (see Figure 4), implying that the magnetothermal mechanism will usually only represent the primary source of instability provided  $\chi > 10^{-1}$ , i.e., under magnetised conditions.

## VI. APPROXIMATE PEAK GROWTH-RATE

When considering the relevance of instability to experimental conditions, it is often useful to have a means of approximating peak wave-numbers  $k_M$  and growth-rates  $\gamma_M(k_M)$ . Sadly, given both the number of free parameters in the dispersion relations (Eqs. (17) and (18)) and the complication of solving for the complex-roots, providing an analytic approximation is not possible for the general magnetothermal instability analysis introduced here. Nevertheless, density length scales  $L_n$  are often much longer than those associated with the magnetic field  $L_B$ , i.e.,  $\Lambda_B \approx 1$ , and in these cases, progress towards an approximate solution can be made for those conditions under which the magnetothermal instability source term dominates over the field generating mechanism. In these cases, the  $S_G$  source term may be neglected and the cut-off wave-number in the CT regime becomes

$$K_{CT}^2 \approx K_c^2 = \frac{S_P^2}{4} \left( 1 + \frac{D_R L_T}{A_N L_B} \right) \left( 1 - \frac{D_T L_T}{A_N L_B} \right) \times \left( \frac{1}{D_T + D_R} \right)^2 \left[ \frac{1}{4D_T D_R - S_E} \right], \quad (30)$$

which is identical to our previous result.<sup>14</sup> Crucially, these assumptions allow us to write the peak instability growth-rates and wave-numbers in terms of two dimensionless functions,  $f_M \equiv f_M(\chi, L_T/L_B, \Lambda, K_M L_T)$  and  $g_M \equiv g_M(\chi, L_T/L_B, \Lambda)$ , each taking arguments given by the parameters  $\chi$ ,  $\Lambda$ , and  $L_T/L_B$ , i.e.,<sup>33</sup>

$$\gamma_M = \frac{f_M}{\tau_T} \left( \frac{\lambda_T}{l_T} \right)^2 \text{ and } k_M = \frac{g_M}{\lambda_T} \left( \frac{\lambda_T}{l_T} \right). \quad (31)$$

These equations highlight the importance of steep temperature gradients to the magnetothermal instability, through the inverse proportionality of  $\gamma_M$  to  $l_T^2$ , while plotting numerically solved values for  $f_M$  and  $g_M$  (see Figure 5) demonstrates the need for intermediate Hall parameter to maximise the value of the source  $S_P$ .

The dimensionless form of Eq. (31) indicates the relevance of the instability to a range of self-similar regimes, and in the absence of alternative methods for predicting peak growth-rates and wave-numbers (and as we shall demonstrate in Sec. VII), both may be used to estimate the relevance of the instability to different conditions. [Note: the following formulae provide a convenient means of calculating the parameters in their arguments:

**Coulomb Logarithm:**  $\log \Lambda_{ei}$

$$\approx 6.9 - \log \left( \frac{Z}{10} \right) + \frac{3}{2} \log \left( \frac{T_e}{\text{keV}} \right) - \frac{1}{2} \log \left( \frac{n_e}{10^{21} \text{cm}^{-3}} \right), \quad (32)$$

**Thermal Mean-free-path:**  $(\lambda_T / \mu\text{m})$

$$\approx 3 \left( \frac{\log \Lambda_{ei}}{5} \right)^{-1} \left( \frac{Z}{10} \right)^{-1} \left( \frac{n_e}{10^{21} \text{cm}^{-3}} \right)^{-1} \left( \frac{T_e}{\text{keV}} \right)^2, \quad (33)$$

**Thermal Collision Time:**  $(\tau_T / \text{ps})$

$$\approx \frac{1}{6} \left( \frac{\log \Lambda_{ei}}{5} \right)^{-1} \left( \frac{Z}{10} \right)^{-1} \left( \frac{n_e}{10^{21} \text{cm}^{-3}} \right)^{-1} \left( \frac{T_e}{\text{keV}} \right)^{3/2}, \quad (34)$$

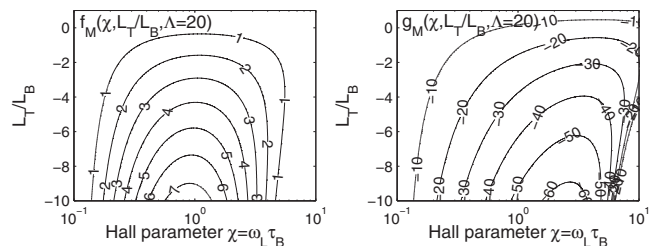


FIG. 5. Contour plots of the functions  $f_M$  (left) and  $g_M$  (right) used to calculate peak growth-rates in Eq. (31).

**Hall Parameter:**  $\chi$

$$= \frac{3\sqrt{\pi}}{4} \left( \frac{\lambda_T}{\mu\text{m}} \right) \left( \frac{\mu\text{m}}{r_L} \right) \approx \frac{1}{4} \left( \frac{\tau_T}{\text{ps}} \right) \left( \frac{|\mathbf{B}|}{\text{T}} \right) \text{ and} \quad (35)$$

**Ratio of Mean-free-path to Skin-depth:  $\Lambda$**

$$\approx 18 \left( \frac{n_e}{10^{21} \text{cm}^{-3}} \right)^{-1/2} \left( \frac{Z}{10} \right)^{-1} \left( \frac{\log \Lambda_{ei}}{5} \right)^{-1} \left( \frac{T_e}{\text{keV}} \right)^2, \quad (36)$$

with  $T_e, n_e, \lambda_T, r_L = c_B \lambda_T / \chi, \tau_T$  and  $|\mathbf{B}|$  measured in keV,  $10^{21} \text{cm}^{-3}$ ,  $\mu\text{m}$ ,  $\mu\text{m}$ , ps, and Tesla, respectively.]<sup>33</sup>

Naturally, such an approach neglects the contributions due to the field generating source term  $S_G$  and other effects arising from hydrodynamics. Nevertheless, neither of these weaknesses should deter estimation: indeed, we expect the magnetothermal mechanism to be relatively dominant over the generating source for intermediate magnetisation (see Sec. V), and peak growth-rates are comparable in both CT and HD regimes (see Sec. III B).

In the following section, therefore, we briefly describe a number of experimental contexts in which the magnetothermal instability could be active and calculate approximate values for both its characteristic growth-rate  $\gamma_M$  and wavelength  $\lambda_M = 2\pi/k_M$ . Before proceeding, however, it is worth making a final remark about the cut-off wave-number  $K_c$ . Since this represents the cut-off when only the magnetothermal mechanism is active, and because we require  $K_c \in \mathbb{R}$ , Eq. (30) implies

$$1 \approx A_N/D_T > L_T/L_B > -A_N/D_R, \quad (37)$$

which is a necessary condition for magnetothermal instability based on the ratio of the length-scales.

## VII. EXPERIMENTAL RELEVANCE

The conditions of Froula *et al.*<sup>9</sup> simulated here provide an obvious case of relevance for the magnetothermal instability, with characteristic wavelengths  $\lambda_M = 2\pi/k_M \sim 40 \mu\text{m}$  and peak growth times  $t_M = 1/\gamma_M \sim 50 \text{ps}$ , well within the nanosecond time-scale of the experiment. One consequence of the instability in this context is the deformation of thermal energy profiles. Indeed, by periodically concentrating the radial heat-flow into “fingers”, the instability enhances the spread of thermal energy (see Figure 1), possibly undermining Froula’s proposal of using fields to suppress non-local heat-transport.<sup>9</sup> This effect can be characterised by comparing temperature profiles from one-dimensional (and thus stable) simulations, with those derived from two-dimensional unstable runs. Indeed, for planar simulations, with a perturbation in the  $y$ -direction, average profiles can be found by calculating the mean temperature for each  $x$  cross-section. Adopting this approach for an 8 T magnetised plasma, after 900 ps of heating we find increased spreading of energy relative to the stable case and cooling of the central region (see Figure 6).<sup>33</sup> Intriguingly, Froula *et al.* detected a similar signature in their experimental data.<sup>9</sup>

Though the magnetothermal instability may increase thermal transport relative to stable scenarios, the imposition

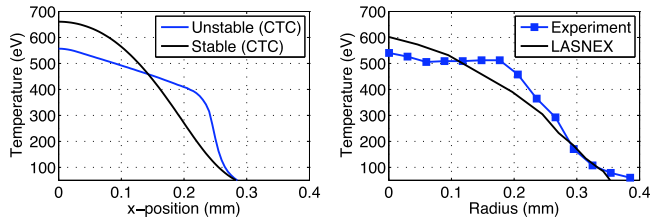


FIG. 6. Temperature profiles calculated by CTC simulation (left) and results sourced from Froula’s investigation<sup>9</sup> (right), demonstrating cooling of the central region due to instability while the laser is at full power.<sup>33</sup> The CTC data are taken after 900 ps heating of a plasma initially magnetised at 8 T: from one-dimensional simulation in the stable case (black curve); and from conditions identical to those of our original paper in the unstable case (blue curve).<sup>14</sup> Note that in these simulations, we use our transport code without hydrodynamic flow, so that thermal spreading derives from the instability rather than compressional cooling. Froula’s data are from investigation of a 12 T plasma after 1.6 ns of heating in cylindrical geometry: both one-dimensional lasnex simulation (black curve) and experiment (blue squares).<sup>9</sup>

of magnetic fields in Froula’s experiment nevertheless reduces thermal flux when compared with unmagnetised conditions, leading to higher temperatures near the laser-spot.<sup>9</sup> Froula *et al.* exploited this effect with some success to create “plasma channels,” using an experimental arrangement and applied fields effectively identical to that of their heat-flow investigation above,<sup>10</sup> though for this subsequent study, both helium ( $Z = 2$ ) and nitrogen ( $Z = 7$ ) gas-jets were probed. Despite the difference in number density  $n_e$  and atomic number  $Z$  for these media, peak wavelengths and growth-rates of the magnetothermal instability are similar in each (see Table V), suggesting that the instability could compromise the formation of smooth plasma channels.

The conditions relevant to Froula’s experiments are well suited to simulation by both CTC and its hydrodynamic counterpart CTC+ and warrant further numerical investigation in cylindrical geometry. The remainder of this section, therefore, is devoted to more speculative estimates of the magnetothermal instability’s possible impact under conditions in which magnetic fields are self-generated: first, to experiments by Li *et al.* designed to study magnetic field structures on the surface of plasma bubbles;<sup>11–13</sup> and second, to both inertial confinement<sup>3–5</sup> and magneto-inertial fusion.<sup>6–8</sup> However, these preliminary estimates based on Eq. (31), and which assume  $l_T \sim -l_B$ , should be treated with some caution. They are summarised alongside those for Froula’s work<sup>9,10</sup> in Table V.

### A. Field structures on the surfaces of plasma bubbles

Unlike Froula’s experiments, in which large fields were imposed on a uniform gas-jet, Li *et al.*<sup>11,12</sup> studied the evolution of magnetic fields self-generated on the surface of plasma bubbles. In Li’s case, the plasma is formed by irradiating a plastic foil (CH,  $Z = 3.5$ ) with a nanosecond laser-pulse of intensity  $\sim 10^{14} \text{ Wcm}^{-2}$  focused to an  $800 \mu\text{m}$  spot: during the illumination phase ( $\lesssim 1 \text{ ns}$ ), plasma is blown from the foil as an hemispherical bubble and continues to expand—preserving approximate cylindrical symmetry co-axial with the beam—after the laser is turned off ( $\gtrsim 1 \text{ ns}$ ). Li *et al.* measured strong fields  $\sim 0.3 \text{ MG} = 30 \text{ T}$  along the surface

TABLE V. Estimated growth-times  $t_M = 1/\gamma_M$  and characteristic wavelengths  $\lambda_M = 2\pi/k_M$  for the magnetothermal instability in various experimental contexts (with parameters sourced from the relevant references as indicated in the first column). Excepting M.I.F., for which  $l_T/l_B \sim 0.5$  is used, we assume the antiparallel relationship  $-l_T \sim l_B$ .

Conditions (Units)	$T_e$ (keV)	$B$ (T)	$n_e$ ( $10^{21}\text{cm}^{-3}$ )	$Z$	$l_T$ ( $\mu\text{m}$ )	$\chi$ (n/a)	$\Lambda$ (n/a)	$\lambda_T$ ( $\mu\text{m}$ )	$r_L$ ( $\mu\text{m}$ )	$\tau_T$ (ps)	$\gamma_M$ ( $\text{ns}^{-1}$ )	$t_M$ (ps)	$k_M$ ( $\mu\text{m}^{-1}$ )	$\lambda_M$ ( $\mu\text{m}$ )
Froula <i>et al.</i> <sup>9</sup>	0.4	4	0.015	7	150	2.5	20	30	16	2.5	20	50	0.16	40
Froula <i>et al.</i> <sup>10</sup>	0.2	3	0.00075	2	200	40	70	400	13	50	10	100	0.25	25
Li <i>et al.</i> <sup>13</sup>	0.4	10	0.0035	3.5	100	45	75	200	6	20	25	40	0.63	10
I.C.F. <sup>4</sup>	2.5	40	0.25	2	300	60	550	200	4.5	10	50	20	1.3	5
M.I.F. <sup>7,8</sup>	1.0	1000	200	1	5	2	10	0.1	0.07	0.006	15	70	1.3	5

of the bubbles and periodic modulation in the magnetic field structure, perpendicular to both the field and temperature gradients, conditions under which we expect the magnetothermal instability to be active.<sup>11,12</sup>

Li's initial studies were mainly of observational importance,<sup>11,12</sup> and it was only in later work that a mechanism for field modulations in terms of magneto-hydrodynamic instability was proposed.<sup>13</sup> The model itself shall not be considered here, but we note that its linear phase predicts growth-rates  $\sim 1 \text{ ns}^{-1}$ ; since these are insufficient to explain the magnitude of the structures over the  $\sim 2 \text{ ns}$  experimental time-scale, Li *et al.* reference secondary "explosive" non-linear processes which they do not fully describe. However, after reducing the field strength estimate to 10 T (to account for generation up to 30 T), the group's parameters suggest that the magnetothermal instability would have a characteristic growth-rate  $\gamma_M \sim 25 \text{ ns}^{-1}$  and wavelength  $\lambda_M \sim 10 \mu\text{m}$  in this context and could account for the field structure without appeal to secondary mechanisms (see Table V). Indeed, this value for  $\lambda_M$  compares well with the characteristic instability length-scale of  $10 \mu\text{m}$  seen in simulations of the bubble.<sup>13</sup> Nevertheless, since the fields in this experiment are azimuthal, magnetic tension could act to stabilise the magnetothermal mechanism. Further work is needed to assess the robustness of our model outside planar geometry.

## B. Inertial confinement and magneto-inertial fusion

Estimates for the magnetothermal instability growth-rates under I.C.F. conditions may be made based on computational data. Indeed, using values taken from simulations of a methane filled hohlraum ( $\text{CH}_4, Z = 2$ ) by Glenzer *et al.*<sup>4</sup>—which show magnetic field structures of approximately 0.4 MG = 40 T extending over scales of  $> 0.5 \text{ mm}$ —Eqs. (31) predict  $\gamma_M \sim 50 \text{ ns}^{-1}$ , with characteristic wavelength  $\lambda_M \sim 5 \mu\text{m}$  (see Table V). These values suggest the instability could impact during nanosecond heating of the hohlraum.

For M.I.F. studies, in which magnetic-fields are directly imposed on the imploding target, there exist more detailed simulation data concerning field gradients.<sup>6–8</sup> Following a 4ns implosion of the target—to compress both the seed field and Deuterium fuel ( $\text{D}_2, Z = 1$ )—electron temperature and field gradients are parallel, with  $l_T \sim 5 \mu\text{m}$  and  $l_B \sim 10 \mu\text{m}$ .<sup>7,8</sup> Since this makes  $l_T/l_B \sim 0.5$ , M.I.F. conditions, post implosion are very much on the border of the  $1 > l_T/l_B$  requirement for magnetothermal relevance (see inequality (37)). Calculating the instability growth-rates and characteristic wavelength

for these parameters, we find  $\gamma_M \sim 15 \text{ ns}^{-1}$  and  $\lambda_M \sim 5 \mu\text{m}$ . However, owing to the sensitivity of this estimate to the value of  $l_T/l_B$ , and because the M.I.F. hotspot radius  $\sim 10 \mu\text{m}$  is comparable to  $\lambda_M$ , the impact of the magnetothermal instability in this context is somewhat questionable. Sadly, there is insufficient data to assess its relevance during the compression phase when inequality (37) may be more easily satisfied.

## C. Kinetic effects

When compared to the electron thermal Larmor radius  $r_L = c_B \lambda_T / \chi$ , the relatively small wavelengths corresponding to the peak instability wave-numbers mean that non-local transport is relevant to the experiments summarised in Table V; indeed, we expect non-local effects to become important whenever  $|k_M r_L| \gtrsim 1$ . Though the physical mechanism of the instability remains the same under these conditions, non-locality is expected to reduce the predictive power of our theory by modifying the values of the transport coefficients. Nevertheless, simulation using our kinetic code IMPACT (see Figure 7) in the context of Froula's experiment<sup>9</sup> shows that this reduction is not serious: the peak growth-rate and cut-off wave-number agree to within approximately 35% and 25% respectively, while the peak wave-number is effectively unchanged. In fact, steeper temperature gradients in the kinetic runs actually make the instability grow faster than in the CTC+ simulations shown in Figures 2 and 3. Consequently, though non-locality should be considered in greater detail as future work, the growth-rates given in Table V probably represent realistic estimates.

Inverse bremsstrahlung (I.B.), the dominant mechanism of heating in under-dense plasmas for laser intensities in the range  $10^{14} - 10^{16} \text{ Wcm}^{-2}$ , can introduce an additional

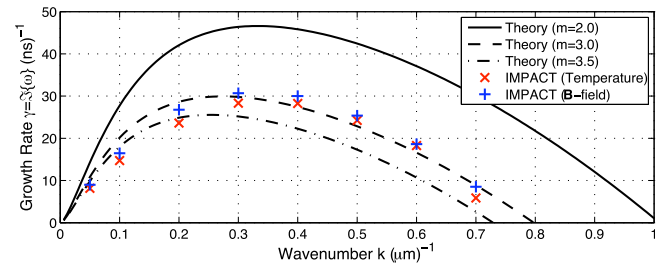


FIG. 7. Comparison between the transport theory of the instability (solid and dashed curves) and growth-rates measured from kinetic simulation of a 6 T plasma using IMPACT (red and blue crosses). Here, the theoretical dispersion curves are calculated from impact profiles at the cross-section  $x \approx 120 \mu\text{m}$  after 500 ps of heating and using a range of super-Gaussian powers  $m$  [IMPACT data from our original paper].<sup>14</sup>

kinetic effect in long-pulse (nanosecond) laser-plasma interactions, even when non-locality is suppressed.<sup>31</sup> Indeed, I.B. preferentially heats the more collisional, slower moving electrons, reducing their number and increasing the population of electrons with intermediate velocity  $v$ . This effect simultaneously flattens and broadens the distribution function  $f_0$  away from a Gaussian  $f_0 \propto \exp(-[v/v_T]^2)$  towards a super-Gaussian, that is,  $f_0 \propto \exp(-[v/\alpha_e v_T]^m)$ , where  $m \in [2, 5]$  and  $\alpha_e$  is a function of  $m$ , thereby altering the transport coefficients. Indeed, Ridgers *et al.*<sup>31</sup> demonstrated that in Froula's experiment,<sup>9</sup> the super-Gaussian power lies in the range  $3.3 > m > 2.0$  as the distance from the laser spot centre is increased. Fortunately, since modified super-Gaussian coefficients have been evaluated,<sup>31</sup> the effects of I.B. heating may be readily included in our calculations of the dispersion relation and compared with kinetic data (see Figure 7). Interestingly, though I.B. does not seem to dramatically suppress instability growth-rates, the theoretical dispersion curves in Figure 7 agree better with the kinetic data when we take  $m = 3.0$  rather than  $m = 2.0$ , suggesting that more work is needed to distinguish between non-local and super-Gaussian effects.

### VIII. SUMMARY AND CONCLUSIONS

We have generalised the theory of the magnetothermal instability<sup>14</sup> to include effects arising from both density gradients and hydrodynamics. By examining two limiting cases—a CT and an HD regime—we showed that it was necessary to modify the theory by introducing the field generating thermal instability source term,<sup>15–20</sup> which can either complement or oppose the magnetothermal mechanism in driving unstable waves (Secs. II and III). The generalised theory was compared favourably with classical transport CTC+ simulations in the context of a nanosecond gas-jet experiment by Froula *et al.*,<sup>9</sup> for which we predict the instability to have characteristic growth-rates and wavelengths of order  $10 \text{ ns}^{-1}$  and  $50 \mu\text{m}$ , respectively, well within the experimental timescales (Sec. IV).

Comparing contributions from the magnetothermal and field generating sources for the conditions of Froula *et al.*,<sup>9</sup> we demonstrated that magnetothermal effects dominate instability in the CT regime and are the only source of unstable feedback in the HD regime (Sec. V). More generally, for magnetised conditions  $\chi > 10^{-1}$  with density length-scales  $L_n$  comparably longer than magnetic field length-scales  $L_B$ , we expect the magnetothermal mechanism to be the primary driver of instability. Indeed, for such conditions we found approximate expressions for both peak instability growth-rates and wave-numbers (Sec. VI). Preliminary calculations based on these expressions suggest that the magnetothermal instability may take effect in both experiments recently conducted by Li *et al.*<sup>11–13</sup> and I.C.F. hohlraums (Sec. VII).

The existence of the magnetothermal instability indicates strongly the need to include both the Nernst effect and Righi-Leduc heat-flow in fluid models of plasmas for which large cross-field heat-flows are expected, especially those at intermediate magnetisation. Growth from noise of the instability's peak modes further implies that such modelling should be two-dimensional. Indeed, planar simulations in

the context of Froula's experiment to suppress non-local heat-flow<sup>9</sup> demonstrate that the instability enhances thermal energy transport relative to one-dimensional (stable) runs, prematurely cooling the laser-heated region while the laser is at full power. It is possible that such a signature could be used to gather experimental evidence of the instability's onset.

Our model of the magnetothermal instability assumes a Cartesian geometry in which fields  $\mathbf{B}$  are perpendicular to both vector quantities  $\mathbf{A}$  and the gradients of scalars  $f$ , that is,  $\mathbf{B} \cdot \mathbf{A} = \mathbf{B} \cdot \nabla f = 0$ . Further theoretical refinement is needed to better assess the instability's consequences for experiments in which this condition does not hold. For example, the inclusion of both planar and curved fields would allow us to assess the importance of magnetic tension and presumably yield more accurate estimates of instability growth-rates in laser-plasmas with azimuthal field geometries, and possibly even more diverse applications, such as Z-pinches. Kinetic effects are also likely to be significant; indeed, the IMPACT simulations presented here already suggest some role for non-locality. Crucially, however, our current model predicts that the instability will be most active when the ratio of the thermal mean-free path  $\lambda_T$  to the temperature length-scale  $l_T$  is relatively large (i.e., steep temperature gradients); in principle, therefore, both non-locality and anisotropic pressure should be included in future studies.<sup>33</sup>

- <sup>1</sup>S. I. Braginskii, Rev. Plasma Phys. **1**, 205 (1965).
- <sup>2</sup>A. Nishiguchi, T. Yabe, and M. G. Haines, Phys. Fluids **28**, 3683 (1985).
- <sup>3</sup>J. Lindl, P. Amendt, R. L. Berger, S. G. Glendinning, S. H. Glenzer, S. W. Haan, R. L. Kauffman, O. L. Landen, and L. J. Suter, Phys. Plasmas **11**, 339 (2004).
- <sup>4</sup>S. H. Glenzer, W. E. Alley, K. G. Estabrook, J. S. D. Groot, M. G. Haines, J. H. Hammer, J.-P. Jadaud, B. J. MacGowan, J. D. Moody, W. Rozmus, L. J. Suter, T. L. Weiland, and E. A. Williams, Phys. Plasmas **6**, 2117 (1999).
- <sup>5</sup>P. M. Nilson, L. Willingale, M. C. Kaluza, C. Kamperidis, S. Minardi, M. S. Wei, P. Fernandes, M. Notley, S. Bandyopadhyay, M. Sherlock, R. J. Kingham, M. Tatarakis, Z. Najmudin, W. Rozmus, R. G. Evans, M. G. Haines, A. E. Dangor, and K. Krushelnick, Phys. Rev. Lett. **97**, 255001 (2006).
- <sup>6</sup>O. Gotchev, N. Jang, J. Knauer, M. Barbero, R. Betti, C. Li, and R. Petrasso, J. Fusion Energy **27**, 25 (2008).
- <sup>7</sup>O. V. Gotchev, P. Y. Chang, J. P. Knauer, D. D. Meyerhofer, O. Polomarov, J. Frenje, C. K. Li, M. J.-E. Manuel, R. D. Petrasso, J. R. Rygg, F. H. Séguin, and R. Betti, Phys. Rev. Lett. **103**, 215004 (2009).
- <sup>8</sup>J. P. Knauer, O. V. Gotchev, P. Y. Chang, D. D. Meyerhofer, O. Polomarov, R. Betti, J. A. Frenje, C. K. Li, M. J.-E. Manuel, R. D. Petrasso, J. R. Rygg, and F. H. Séguin, Phys. Plasmas **17**, 056318 (2010).
- <sup>9</sup>D. H. Froula, J. S. Ross, B. B. Pollock, P. Davis, A. N. James, L. Divol, M. J. Edwards, A. A. Offenberger, D. Price, R. P. J. Town, G. R. Tynan, and S. H. Glenzer, Phys. Rev. Lett. **98**, 135001 (2007).
- <sup>10</sup>D. H. Froula, L. Divol, P. Davis, J. P. Palastro, P. Michel, V. Leurent, S. H. Glenzer, B. B. Pollock, and G. Tynan, Plasma Phys. Controlled Fusion **51**, 024009 (2009).
- <sup>11</sup>C. K. Li, F. H. Séguin, J. A. Frenje, J. R. Rygg, R. D. Petrasso, R. P. J. Town, P. A. Amendt, S. P. Hatchett, O. L. Landen, A. J. Mackinnon, P. K. Patel, M. Tabak, J. P. Knauer, T. C. Sangster, and V. A. Smalyuk, Phys. Rev. Lett. **99**, 015001 (2007).
- <sup>12</sup>C. K. Li, F. H. Séguin, J. A. Frenje, J. R. Rygg, R. D. Petrasso, R. P. J. Town, O. L. Landen, J. P. Knauer, and V. A. Smalyuk, Phys. Rev. Lett. **99**, 055001 (2007).
- <sup>13</sup>C. K. Li, J. A. Frenje, R. D. Petrasso, F. H. Séguin, P. A. Amendt, O. L. Landen, R. P. J. Town, R. Betti, J. P. Knauer, D. D. Meyerhofer, and J. M. Soures, Phys. Rev. E **80**, 016407 (2009).
- <sup>14</sup>J. J. Bissell, C. P. Ridgers, and R. J. Kingham, Phys. Rev. Lett. **105**, 175001 (2010).

- <sup>15</sup>D. Tidman and R. Shanny, *Phys. Fluids* **17**, 1207 (1974).
- <sup>16</sup>L. A. Bol'shov, Y. A. Dreizin, and A. M. Dykhne, *JETP Lett.* **19**, 168 (1974).
- <sup>17</sup>J. H. Brownell, *Comments on Plasma Phys. Controlled Fusion* **4**, 131 (1979).
- <sup>18</sup>M. Ogasawara, A. Hirao, and H. Ohkubo, *J. Phys. Soc. Jpn.* **49**, 322 (1980).
- <sup>19</sup>A. Hirao and M. Ogasawara, *J. Phys. Soc. Jpn.* **50**, 668 (1981).
- <sup>20</sup>A. Fruchtman and H. R. Strauss, *Phys. Fluids B: Plasma Phys.* **4**, 1397 (1992).
- <sup>21</sup>E. S. Weibel, *Phys. Rev. Lett.* **2**, 83 (1959).
- <sup>22</sup>E. M. Epperlein, *Plasma Phys. Controlled Fusion* **27**, 1027 (1985).
- <sup>23</sup>M. G. Haines, *J. Plasma Phys.* **12**, 1 (1974).
- <sup>24</sup>M. G. Haines, *Phys. Rev. Lett.* **47**, 917 (1981).
- <sup>25</sup>T. J. M. Boyd and J. J. Sanderson, *The Physics of Plasmas* (Cambridge University Press, 2005).
- <sup>26</sup>R. P. Drake, *High-Energy-Density Physics* (Springer, 2006).
- <sup>27</sup>J. R. Davies, M. Fajardo, M. Kozlova, T. Mocek, J. Polan, and B. Rus, *Plasma Phys. Controlled Fusion* **51**, 035013 (2009).
- <sup>28</sup>M. G. Haines, *Can. J. Phys.* **64**, 912 (1986).
- <sup>29</sup>E. M. Epperlein, *J. Phys D* **17**, 1823 (1984).
- <sup>30</sup>E. M. Epperlein and M. G. Haines, *Phys. Fluids* **29**, 1029 (1986).
- <sup>31</sup>C. P. Ridgers, A. G. R. Thomas, R. J. Kingham, and A. P. L. Robinson, *Phys. Plasmas* **15**, 092311 (2008).
- <sup>32</sup>M. G. Haines, *Plasma Phys. Controlled Fusion* **28**, 1705 (1986).
- <sup>33</sup>J. J. Bissell, "Magnetised transport and instability in laser produced plasmas," Ph.D. thesis, Imperial College London, 2011.